



# Multiscale framework for behavior prediction in granular media

José E. Andrade\*, Xuxin Tu

*Theoretical & Applied Mechanics, Northwestern University, Evanston, IL 60208, USA*

## ARTICLE INFO

### Article history:

Received 19 November 2008

## ABSTRACT

In this work, a predictive multiscale framework for modeling the behavior of granular materials is presented. The method is particularly attractive due to its simplicity and ability to exploit the existing finite element and computational inelasticity technologies. Furthermore, this semi-concurrent multiscale method extracts two key material parameters from the granular structure: dilatancy and frictional resistance. The evolution of these material parameters is upscaled into classical two- and three-invariant plasticity models, effectively bypassing phenomenological hardening laws. The predictiveness of the method is clearly demonstrated by comparing its performance with experimental results and direct numerical simulations under homogeneous and inhomogeneous conditions. The high-quality predictions obtained using the multiscale method highlight its potential to unravel complex material behavior where hitherto phenomenological models have failed.

© 2009 Elsevier Ltd. All rights reserved.

## 1. Introduction

Granular matter is ubiquitous in nature and engineering and appears in a plethora of presentations including sands, sandstones, concrete, pharmaceutical pills, and nanoparticles, just to name a few. In order to understand and predict the behavior of granular materials, one must recognize that their mechanical behavior is fundamentally encoded at the granular scale. The macroscopic response of granular matter is governed by relative particle rolling and sliding, the expulsion of interstitial fluids and, at high pressures, grain comminution (i.e., crushing under extreme pressure). An accurate model for granular materials must be able to capture most of these extremely complex, yet crucial, features. Phenomenological plasticity models have typically been proposed to approximate the aforementioned physics at larger scales. Many key macroscopic features of granular behavior can be successfully captured by phenomenological models: irreversible deformations, pressure-dependence, density-dependence, dilatancy, nonassociative plastic flow, Bauschinger effect, etc. Examples of plasticity models that capture one or more of these effects abound in the literature (Collins, 1990; Harris, 1992; Kingston and

Spencer, 1970; DiMaggio and Sandler, 1971; Dafalias and Popov, 1975; Vermeer and de Borst, 1984). These models have a place in science and engineering due to their ability to represent the macroscopic behavior of the material under relatively well controlled and homogeneous conditions. However, some emerging scientific and engineering challenges require a deeper understanding of the material and highlight the limitations inherent in the phenomenological approach.

For example, the important issue of catastrophic instabilities such as landslides and liquefaction in sands raises significant challenges for purely phenomenological models. Efforts have been made to predict the onset of these instabilities using bifurcation theory (Rudnicki and Rice, 1975; Borja, 2002; Borja, 2006; Andrade, 2009); however, it is well-known that the prediction of bifurcation is sensitive to the constitutive model used in the analysis. Furthermore, it is not clear how the material behaves *after* the onset of the instabilities. For example, shear bands in sands induce large deformations that will certainly lead to the development of load chains (i.e., columns of grains carrying loads) and enhanced material rate-dependence, a feature that most phenomenological models for sand currently ignore (Rechenmacher, 2006; Oda et al., 2004; Hartley and Behringer, 2003; Mueth, 2003). In addition, during liquefaction, the soil transitions from solid to

\* Corresponding author.

E-mail address: [j-andrade@northwestern.edu](mailto:j-andrade@northwestern.edu) (J.E. Andrade).

fluid-like behavior, which also leads to very large strains and rate-effects. How can a phenomenological model transition after the onset of instabilities to capture the emerging physics?

One possible answer to the aforementioned questions is to rely on grain scale techniques. Particle mechanics models (similar to molecular dynamics models) can answer many of the questions in a fundamental way. This was certainly the motivation behind the pioneering work of [Cundall and Strack \(1979\)](#) when the discrete element method (DEM) was invented. Since its inception, DEM has been used to investigate the micromechanical features of granular behavior ([Cambou, 1998](#); [Oda et al., 1999](#)). In general, grain scale mechanical models have captured the attention of many researchers and have been used to model a plethora of materials, such as rocks ([Barbosa-Carrillo et al., 1990](#)), asphalt mixtures ([You, 2003](#)), concrete ([Tavarez, 2005](#)), and clays ([Anandarajah, 1999](#)). Industrial applications include the modeling of chemical particles ([Deen et al., 2007](#)), powders ([Sheng et al., 2004](#)) and nanoparticles ([Severson, 2007](#)). The granular approach has also been used to investigate the effect of shape (especially on the dilatancy properties of granular materials), including polyhedral blocks ([Cundall, 1988](#)), ellipsoids ([Lin and Ng, 1997](#)), oblate/prolate ovoids ([Kuhn, 2003](#)), and arbitrary shapes using overlapping rigid clusters ([Sallam, 2004](#)). From a physics perspective, the effect of relative density on compaction processes ([Procopio and Zavalangos, 2005](#)) and the fluctuations in particle interactions due to uniaxial loading ([Ma and Zhang, 2006](#)) have been successfully studied using grain scale models. Engineering applications include penetration of concrete targets ([Tavarez and Plesha, 2007](#)), generation of constitutive relations for granular materials ([Borja and Wren, 1995](#); [Wellmann et al., 2008](#)), investigation of the microscopic mechanism of shear banding ([Bardet and Proubet, 1991](#)), simulation of fluidized beds widely used in chemical and industrial applications ([Deen et al., 2007](#)), and the important problem of particle crushing ([McDowell et al., 1996](#); [Marketos and Bolton, 2007](#)).

Unfortunately, grain scale (or discrete) models suffer from two major shortcomings. Firstly, discrete models are prohibitively expensive for computing mechanical behavior at the meter-scale. In fact, the computational power needed to realistically achieve engineering scale problems will likely not be available for two decades ([Cundall, 2001](#)). Currently, modelers have to resort to enlarging the particles and calibrating the model to capture the expected behavior. The second shortcoming relates to this last observation: the enlargement of particles and the use of smooth particles such as spheres and ellipsoids renders the model as just another phenomenological method, where parameters – albeit physically intuitive – are tuned to capture the desired behavior ([Tu and Andrade, 2008](#)). Particle angularity and relevant scales cannot be accurately modeled by classical discrete methods at this point. Consequently, it is clear that a predictive multiscale approach combining the strengths of the available continuum and discrete methods is a critical need.

Multiscale methods are clearly needed to ameliorate the bottleneck resulting from the high computational power required by discrete methods and also to enhance,

and perhaps bypass, phenomenological plasticity models. Multiple scale methods generally imply the utilization of information at one length scale to subsequently model the response of the material at larger length scales ([Liu et al., 2006](#)). These methods are typically classified as hierarchical or concurrent. Hierarchical methods use information from the smaller scale as input for the larger scale. On the other hand, concurrent methods run models at different scales simultaneously.

Multiscale approaches were born as a means for obtaining constitutive responses without resorting to pure phenomenology. The pioneering Quasi-Continuum method proposed the use of the so-called Cauchy–Born rule to obtain a continuum energy density function from molecular dynamics computations within a finite region of interest ([Tadmor et al., 1996](#)). Another similar multiscale method is the recently proposed Virtual Power Domain Decomposition ([Liu and McVeigh, 2008](#)), which has been used to do concurrent and hierarchical simulations in solids with heterogeneities at multiple scales. Very recently, a  $FE^2$  algorithm was proposed by [Belytschko et al. \(2008b\)](#) to aggregate discontinuities across scales in highly distorted areas in solids. Even though the method has only been used within a continuum formulation so far, it promises to link particulate or molecular dynamics with continuum mechanics. Unfortunately, none of the aforementioned methods have focused on granular materials within a multiscale framework.

In this work, we present a semi-concurrent multiscale method to extract the behavior of granular materials directly from the granular structure. The method is labeled after the taxonomy proposed by [Belytschko et al. \(2008a\)](#) where they describe semi-concurrent methods as those in which the fine scale model is weakly coupled to the macro scale model, but information is passed back and forth. This is the methodology used in the proposed multiscale scheme. The central idea is to bypass the phenomenological evolution of material parameters necessitated by the plasticity models by extracting such evolutions from the grain scale and upscaling them into the continuum model. Classical plasticity models used in simulating material behavior are utilized. The Drucker–Prager model ([Drucker and Prager, 1952](#)) and a smooth version of the Mohr–Coulomb model furnished by the Matsuoka–Nakai model ([Matsuoka and Nakai, 1982](#)) are utilized as prototypes. Both of these models necessitate the evolution of the dilatancy and frictional resistance. Typically, the evolution of these parameters is governed by a phenomenological hardening law. In this work, these parameters are extracted semi-concurrently from the granular scale and used in the continuum scale computations. As pointed out by [Reynolds \(1885\)](#) in his seminal paper, the dilatancy plays a crucial role in describing the behavior of granular matter. Since the multiscale model is ultimately an isotropic plasticity model, the method enjoys all the advantages available to continuum plasticity methods and exploits all the finite element technology available as well.

The organization of the paper is as follows. Section 2 describes the continuum plasticity models and the main ingredients involved for a typical isotropic formulation. The role of the hardening modulus is clearly underscored

in this section. Also, an overview of granular scale techniques is presented. In particular, the DEM and advanced experimental techniques amenable to the proposed multiscale method are briefly described. Then, Section 3 describes in detail the main ideas behind the proposed multiscale technique and the type of information that is passed between the granular scale and the continuum scale. Section 4 provides a detailed account on how the multiscale method is implemented numerically within the context of a nonlinear finite element code and a stress-integration algorithm. Finally, the predictiveness and simplicity of the model are showcased in Section 5, where comparisons are made with physical experiments on sands and direct numerical simulations using DEM. Conclusions are presented at the end of the paper based on the findings in the previous sections.

As for notations and symbols used in this paper, bold-faced letters denote tensors and vectors; the symbol ' $\cdot$ ' denotes an inner product of two vectors (e.g.  $\mathbf{a} \cdot \mathbf{b} = a_i b_i$ ), or a single contraction of adjacent indices of two tensors (e.g.  $\mathbf{c} \cdot \mathbf{d} = c_{ij} d_{jk}$ ); the symbol ':' denotes an inner product of two second-order tensors (e.g.  $\mathbf{c} : \mathbf{d} = c_{ij} d_{ij}$ ), or a double contraction of adjacent indices of tensors of rank two and higher (e.g.  $\mathbf{C} : \boldsymbol{\epsilon}^e = C_{ijkl} \epsilon_{kl}^e$ ); the symbol ' $\otimes$ ' denotes a juxtaposition, e.g.,  $(\mathbf{a} \otimes \mathbf{b})_{ij} = a_i b_j$ . Finally, for any symmetric second order tensors  $\boldsymbol{\alpha}$  and  $\boldsymbol{\beta}$ ,  $(\boldsymbol{\alpha} \otimes \boldsymbol{\beta})_{ijkl} = \alpha_{ij} \beta_{kl}$ ,  $(\boldsymbol{\alpha} \oplus \boldsymbol{\beta})_{ijkl} = \alpha_{ik} \beta_{jl}$ , and  $(\boldsymbol{\alpha} \ominus \boldsymbol{\beta})_{ijkl} = \alpha_{il} \beta_{jk}$ .

## 2. From grain scale physics to continuum formulations

### 2.1. Continuum: isotropic elastoplasticity

Assuming isotropic infinitesimal elastoplasticity as a plausible framework for describing the behavior of granular materials, the following ingredients need to be specified (Simo and Hughes, 1998):

- Additive decomposition of strain rate into elastic and plastic components, i.e.,  $\dot{\boldsymbol{\epsilon}} = \dot{\boldsymbol{\epsilon}}^e + \dot{\boldsymbol{\epsilon}}^p$ .
- Generalized Hooke's law, i.e.,  $\dot{\boldsymbol{\sigma}} = \mathbf{c}^e : \dot{\boldsymbol{\epsilon}}^e$ , where  $\mathbf{c}^e$  is the elastic constitutive tensor.
- Elastic domain and yield condition such that the yield surface  $F = F(\boldsymbol{\sigma}, \boldsymbol{\alpha}) = 0$  defines the limit of the domain, where the vector  $\boldsymbol{\alpha}$  contains the stress-like plastic internal variables.
- Non-associative plastic flow rule, i.e.,  $\dot{\boldsymbol{\epsilon}}^p = \dot{\lambda} \mathbf{g}$ , where  $\dot{\lambda} \geq 0$  is the consistency or optimality parameter and  $\mathbf{g} := \partial G / \partial \boldsymbol{\sigma}$  is the direction of the plastic flow with  $G = G(\boldsymbol{\sigma}, \boldsymbol{\alpha})$  as the plastic potential function.
- The Kuhn–Tucker optimality condition,  $\dot{\lambda} F = 0$ , which induces the consistency requirement  $\dot{\lambda} \dot{F} = 0$ . The consistency condition necessitates the formulation of a hardening law such that  $\partial F / \partial \boldsymbol{\alpha} \cdot \dot{\boldsymbol{\alpha}} = -\dot{\lambda} H$ , where  $H$  is typically dubbed the generalized hardening modulus. The tangent of the yield surface,  $\mathbf{f} = \partial F / \partial \boldsymbol{\sigma}$ , is also required to evaluate the consistency condition.

The aforementioned ingredients furnish an elastoplastic rate constitutive expression as a function of the total strain rate such that

$$\dot{\boldsymbol{\sigma}} = \mathbf{c}^{\text{ep}} : \dot{\boldsymbol{\epsilon}} \quad (2.1)$$

where

$$\mathbf{c}^{\text{ep}} = \mathbf{c}^e - \frac{1}{\chi} \mathbf{c}^e : \mathbf{g} \otimes \mathbf{f} : \mathbf{c}^e, \quad \chi = H + \mathbf{g} : \mathbf{c}^e : \mathbf{f} \quad (2.2)$$

Phenomenology is typically used to derive the aforementioned ingredients for a given isotropic plasticity model based on limited experiments or sometimes physical intuition. At the bare minimum, the yield surface, plastic potential, and hardening modulus need to be specified. In the case of granular materials, one such phenomenological model is proposed by Borja and Andrade (2006) and Andrade and Borja (2006). In this model, as in most others, the greatest degree of uncertainty stems from the hardening modulus. Typically, the hardening law furnishes a rate dependence between the stress-like plastic variables, lumped in the vector  $\boldsymbol{\alpha}$ , and the plastic strain rate, i.e.,  $\dot{\boldsymbol{\alpha}} = \dot{\lambda}(\boldsymbol{\alpha}, \dot{\boldsymbol{\epsilon}}^p)$ . In the case of granular materials, the hardening law attempts to incorporate the micromechanical features encoded at the grain scale in a smeared and averaged way. Hence, it is plausible to aim at extracting the evolution of the stress-like plastic variables directly from the microstructure.

Consider the following three independent invariants of the stress tensor, i.e.,

$$I_1 = \text{tr } \boldsymbol{\sigma}, \quad I_2 = (\mathbf{s} : \mathbf{s})^{1/2} = \|\mathbf{s}\|, \quad I_3 = \det \boldsymbol{\sigma} \quad (2.3)$$

where  $\mathbf{s} = \boldsymbol{\sigma} - 1/3 I_1 \mathbf{1}$  is defined as the deviatoric component of the stress tensor  $\boldsymbol{\sigma}$  and  $\mathbf{1}$  is the second order identity tensor. In what follows, we will consider a class of isotropic plasticity models fully defined in terms of three stress invariants such that  $F(\boldsymbol{\sigma}, \boldsymbol{\alpha}) = F(I_1, I_2, I_3, \boldsymbol{\alpha})$  and  $G(\boldsymbol{\sigma}, \boldsymbol{\alpha}) = G(I_1, I_2, I_3, \boldsymbol{\alpha})$ . The two stress invariant formulation will be considered first as it is useful to present the concepts covered in this paper. Subsequently, the formulation is shown to apply to three stress invariant models as well.

### 2.2. Two-invariant plasticity

Making use of the first two invariants, it is possible to define a generalized yield surface and plastic potential such that

$$F(I_1, I_2, \boldsymbol{\alpha}) = \sqrt{\frac{3}{2}} I_2 + m(I_1, \boldsymbol{\alpha}) - c(\boldsymbol{\alpha})$$

$$G(I_1, I_2, \boldsymbol{\alpha}) = \sqrt{\frac{3}{2}} I_2 + \bar{m}(I_1, \boldsymbol{\alpha}) - \bar{c}(\boldsymbol{\alpha}) \quad (2.4)$$

The functions  $m$  and  $\bar{m}$  control the shape of the yield surface and plastic potential on a meridian plane, respectively. Similarly,  $c$  is a parameter that relates to the degree of cohesion in the material and  $\bar{c}$  is typically used as a free parameter to allow the yield surface and plastic potential to cross at a point  $(I_1, I_2)$ . In general,  $c = 0$  for granular materials as is the case here. Additionally, one can define the local tangents to the yield surface and plastic potential such that

$$\mu = 3 \frac{\partial m}{\partial I_1}, \quad \beta = 3 \frac{\partial \bar{m}}{\partial I_1} \quad (2.5)$$

The physical significance of  $\mu$  is that it relates the allowable increase (or decrease) in shear stress for a given

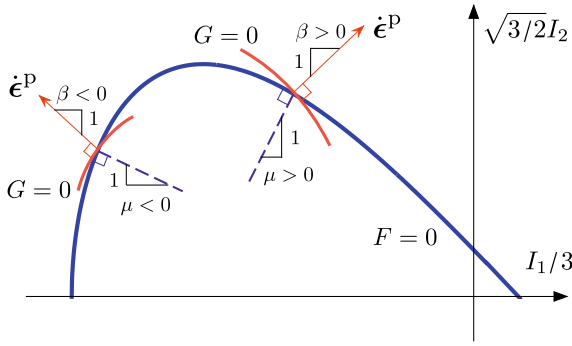


**Fig. 1.** Generalized two-invariant model in invariant space. Note the geometric significance of plastic parameters  $\mu$  and  $\beta$ .

increase in pressure. Similarly,  $\beta$  represents the plastic dilatancy, relating the corresponding increase (or decrease) in plastic shear strain to a given change in plastic volumetric strain. These physical interpretations afford the model a clear connection to the micromechanics. Fig. 1 shows a typical plot of the generalized two invariant formulation and compares the meridian trace of the yield surface and plastic potential. One can further show that

$$\begin{aligned} \mathbf{f} &= \frac{1}{3}\mu\mathbf{1} + \sqrt{\frac{3}{2}}\hat{\mathbf{n}} \\ \mathbf{g} &= \frac{1}{3}\beta\mathbf{1} + \sqrt{\frac{3}{2}}\hat{\mathbf{n}} \end{aligned} \quad (2.6)$$

where  $\mathbf{1}$  is the second order identity tensor and  $\hat{\mathbf{n}} := \mathbf{s}/\|\mathbf{s}\|$  is a unit tensor in the direction of the deviatoric component of  $\boldsymbol{\sigma}$ .

Recalling the flow rule and the definition of the volumetric and deviatoric strains, we obtain

$$\dot{\epsilon}_v^p = \text{tr}\dot{\epsilon}^p = \dot{\lambda}\beta, \quad \dot{\epsilon}_s^p = \sqrt{\frac{2}{3}}\|\dot{\epsilon}^p - 1/3\dot{\epsilon}_v^p\mathbf{1}\| = \dot{\lambda} \quad (2.7)$$

Therefore, the dilatancy  $D = \dot{\epsilon}_v^p/\dot{\epsilon}_s^p = \beta$  and at yield (i.e.,  $F=0$ , which is the case of interest here)  $2\mu = -3\sqrt{6}\partial I_2/\partial I_1$ . A classic example of the above formulation is the Drucker–Prager model, where  $\mu$  and  $\beta$  are considered functions of the plastic strain magnitude such that  $\mu = \mu(\lambda)$  and  $\beta = \beta(\lambda)$ .

For cohesionless materials (i.e.,  $c=0$ ) the classic Drucker–Prager model considers  $\mu$  as a material parameter independent of the stress, such that the formulation reduces to

$$F = \sqrt{\frac{3}{2}}I_2 + \frac{1}{3}\eta I_1 = 0 \quad (2.8)$$

where we note that the local slope  $\mu$  coincides with the stress ratio, i.e.,  $\mu = \eta = -3\sqrt{3/2}I_2/I_1$ , and hence can be interpreted as the frictional resistance or friction coefficient. Furthermore, it is not uncommon to find stress–dilatancy relationships in the literature linking the friction coefficient to the dilatancy angle such that

$$\underbrace{\beta}_{\text{dilatancyresistance}} = \underbrace{\eta}_{\text{frictionresistance}} - \underbrace{\eta_{cv}}_{\text{residualfrictionresistance}} \quad (2.9)$$

where  $\eta_{cv}$  is a constant material parameter measuring the friction coefficient or stress ratio at constant volume (crit-

ical state) in a granular assembly (see Taylor, 1948; Rowe, 1962; Wood, 1990 for examples of typical stress–dilatancy relations in granular media). From the equation above, experimental evidence, and thermodynamic considerations,  $\eta \geq \beta$ . Finally, the evolution of the yield surface due to plastic flow takes the form

$$\frac{\partial F}{\partial \mu} \dot{\mu} = -\dot{\lambda} H \quad (2.10)$$

and hence  $\text{sgn}H = \text{sgn}\dot{\mu}$  (this is a result of  $\partial F/\partial \mu \leq 0$  in most cases). The material is said to be undergoing friction hardening when  $H > 0$  and friction softening if  $H < 0$ . Perfect plasticity is attained when  $H = \dot{\mu} = 0$ .

**Remark 1.** We note that in the cohesionless Drucker–Prager formulation, used herein as the archetype for two-invariant models, the local tangent  $\mu = -3\sqrt{3/2}\partial I_2/\partial I_1$  coincides with the stress ratio  $\eta = -3\sqrt{3/2}I_2/I_1$  and are, therefore, used interchangeably. This, of course, is not necessarily the case for all models. In fact,  $\mu$  can take negative values in general, whereas the stress ratio  $\eta$  cannot. For example, more modern formulations have made the friction coefficient a function of the pressure and some plastic variables such that,

$$\begin{aligned} F &= \sqrt{\frac{3}{2}}I_2 + \frac{1}{3}\eta(I_1, I_1^*)I_1 = 0, \quad \eta(I_1, I_1^*) = M[1 + \ln(I_1^*/I_1)], \\ \mu &= \eta - M \end{aligned} \quad (2.11)$$

where  $\eta_{cv} = M$  is a material constant related to the critical state and  $I_1^*$  is called the image mean stress and controls the size of the yield surface. This formulation was first proposed in the so-called Granta Gravel model (Schofield and Wroth, 1968) and has been used extensively in subsequent models for sands such as Nova and Wood (1979), Jefferies (1993), Borja and Andrade (2006), and Andrade and Borja (2006). The yield surface equation is then allowed to expand by making  $I_1^*$  a function of the plastic strains. The use of the stress–dilatancy relation together with associativity assumptions, provide a complete framework for the integration of stresses in granular media. The evolution of plasticity parameters, such as  $I_1^*$ , has most often been linked to the plastic strain via phenomenological laws (cf. Andrade and Borja, 2006).

### 2.3. Three-invariant plasticity

Considering the three invariants of the stress tensor, Matsuoka and Nakai (1982) proposed a smooth version of the Mohr–Coulomb failure surface. This surface has been very well received as it captures all six corners of the deviatoric projection of the Mohr–Coulomb model, whereas the Drucker–Prager model presented in the previous section can only capture three corners at a given time (either the compression or extension corners but never both). This important feature, often called triaxiality, is observed in many granular materials. Fig. 2 shows experiments on sand where the difference in strength under compression and extension are shown. Also in this figure, the deviatoric projections of the Matsuoka–Nakai and the Drucker–Prager model are shown, where it is obvious that the three

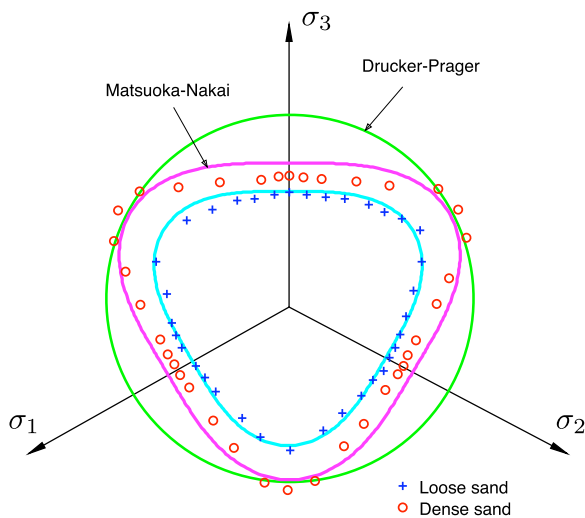


**Fig. 2.** Yield points on deviatoric plane for loose and dense sands. Triaxial nature of strength is underscored by the data and the superior fit of the Matsuoka–Nakai over Drucker–Prager is apparent. Data from Lade and Duncan (1975).

invariant formulation is able to capture the triaxiality feature more accurately.

The Matsuoka–Nakai yield surface and plastic potential read

$$\begin{aligned} F(\boldsymbol{\sigma}, \boldsymbol{\alpha}) &= F(I_1, I_2, I_3, \alpha) = 2I_1^3 - 3I_1I_2^2 - 6I_3\alpha = 0 \\ G(\bar{\boldsymbol{\sigma}}, \bar{\boldsymbol{\alpha}}) &= G(\bar{I}_1, \bar{I}_2, \bar{I}_3, \bar{\alpha}) = 2\bar{I}_1^3 - 3\bar{I}_1\bar{I}_2^2 - 6\bar{I}_3\bar{\alpha} = 0 \end{aligned} \quad (2.12)$$

where  $\bar{I}_A$  for  $A=1,2,3$  are the invariants as defined in 2.3 but for a shifted stress tensor  $\bar{\boldsymbol{\sigma}} = \boldsymbol{\sigma} - \bar{c}\mathbf{1}$  with  $\bar{c}$  as the apparent cohesion. This apparent cohesion serves as a free parameter allowing for the yield surface and plastic potential to intersect (cf. two invariant formulation above). A cohesionless yield surface is presented here for simplicity, but nothing precludes the formulation from accommodating cohesion effects. Finally, the plastic parameters  $\alpha$  and  $\bar{\alpha}$  are related to the inclination of the yield surface and plastic potential, respectively. These parameters are related to the friction and dilatancy angles such that

$$\alpha = \frac{9 - \sin^2 \phi}{1 - \sin^2 \phi}, \quad \bar{\alpha} = \frac{9 - \sin^2 \psi}{1 - \sin^2 \psi} \quad (2.13)$$

where  $\phi$  and  $\psi$  are the friction and dilation angles, respectively. Defining  $\beta_{AVE} = (\beta_C + \beta_E)/2$ , where  $\beta_C$  and  $\beta_E$  are the  $\beta$ -values corresponding to the Drucker–Prager model when it is allowed to fit the compression and extension corners of the Matsuoka–Nakai model, respectively. It is possible to show that  $2\sin \psi \approx \beta_{AVE}$  is the average dilatancy. This approximation is not crucial; it is simply a convenient way of linking the dilatancy angle  $\psi$  with a tangible material quantity such as the dilatancy  $D = \dot{\epsilon}_v^p / \dot{\epsilon}_s^p$ .

As in the two-invariant formulation, a phenomenological law governs the evolution of the yield surface and plastic potential via  $\alpha = \alpha(\lambda)$  and  $\bar{\alpha} = \bar{\alpha}(\lambda)$ . Similarly, the evolution of the friction angle and dilation angle are typically linked via a stress–dilatancy relation (cf. Eq. (2.9))

$$\tan \psi = \tan \phi - \tan \phi_{cv} \quad (2.14)$$

In general, the stress–dilatancy relation boils down to an evolution of dilatancy as a function of friction minus the residual or critical state friction resistance. These relationships are convenient as they provide a direct evolution equation between dilation and friction. The frictional resistance at residual state is considered a constant material parameter. The use of a stress–dilatancy relation allows for introduction of a single hardening law, say  $\alpha = \alpha(\lambda)$ , and then provides the means for the evaluation of the dilatancy parameter. However, the hardening law will have to be postulated based on the phenomenological approach. This is, perhaps, the most problematic ingredient of plasticity models and is a significant source of uncertainty as the model is applied beyond the stress/strain paths used in the development stage.

To summarize, a typical simple plasticity model for cohesionless granular materials, such as those presented above, will require the use of at least three material parameters: two to describe the elastic response (e.g., if linear isotropic elasticity is used one can specify Young's modulus  $E$  and Poisson's ratio  $\nu$ ), and at least one additional plasticity parameter related to the critical or residual state (e.g.,  $\phi_{cv}$ ). However, the use of a hardening law will necessarily introduce at least one more parameter. Therefore, typical models will require at least four material parameters. The first three parameters mentioned above ( $E, \nu, \phi_{cv}$ ) are treated as constants and considered invariant for a particular material. Furthermore, they are not difficult to assess and are relatively straightforward to calibrate for a given material. However, it is well known that material constants related to hardening laws are not straightforward to calibrate and many times require re-calibration when the boundary conditions or packing densities are changed. This is inconvenient and is a source of uncertainty in plasticity models.

Ideal hardening laws would account for changes in fabric (e.g., packing density and coordination number) for a granular assembly. However, as mentioned before, classical hardening laws smear these effects and compute changes in plastic variables on average. New simulation and experimental capabilities open the door to a radical change in paradigm. What if instead of proposing a closed-form expression for the hardening law as a function of the plastic strain (e.g.,  $\alpha = \alpha(\lambda)$ ), the evolution of  $\alpha$  is inferred directly from the microstructure every time an update is necessary? In other words, if  $\alpha$  or  $\bar{\alpha}$  have a clear physical meaning (via their relation to the friction and dilation angle, respectively; cf., Eq. 2.14), why not extract the value of these parameters directly from the evolving microstructure at an area or volume of interest? This was not possible before since we did not have the ability to observe these changes experimentally and multiscale models were not able to extract this information from grain scale simulations. The subsequent sections illustrate how grain scale computations and advanced experimental techniques can be used to extract the evolution of plastic variables used in simple plasticity models such as the ones presented here.



## 2.4. Granular physics: DEM and advanced experimental techniques

As mentioned before, the most basic physical phenomena in granular media are encoded in the grain scale. Based on this premise, many efforts have been made to advance the state of the art in discrete mechanics. The discrete element method (DEM) was developed by [Cundall and Strack \(1979\)](#) to account for the inherently discontinuous and heterogeneous nature of granular materials. The idea was to replace the continuum mechanics formulation plagued by phenomenology and, in the case of rate independent models, pathological mesh dependence post-peak. However, computational expenses have crippled discrete mechanics methods, which are not yet able to resolve the grain scale accurately and have had to resort to the same techniques required to calibrate phenomenological models ([Tu and Andrade, 2008](#)). It is not uncommon to use ‘grains’ of much larger size or mass in order to simulate field scale problems under quasi-static conditions. It is expected that discrete mechanics methods will not reach the ability to predict the behavior of granular systems at a specimen and field scale for the next twenty years ([Cundall, 2001](#)). However, grain scale mechanical models can certainly be used to extract meso scale behavior, which can then be up-scaled by continuum models.

It is important to define the concept of a unit cell at this point. Unlike a representative element volume (REV) the unit cell may not necessarily represent the behavior of the entire domain. However, similar to the concept of REV, the unit cell is defined as a finite physical domain where the continuum is applicable (high frequency oscillations are not present in a given continuum quantity, e.g., dilatancy). Therefore, the unit cell is meaningful at the meso scale and above.

Within the context of unit cell computations, the stress tensor can be obtained by invoking equilibrium conditions ([Christoffersen et al., 1981](#)), i.e.,

$$\bar{\sigma} = \text{sym} \left[ \frac{1}{V} \sum_{n=1}^{N_c} \mathbf{l}^n \otimes \mathbf{d}^n \right] \quad (2.15)$$

where  $\mathbf{l}^n$  represents the contact force at contact point  $n$ ,  $\mathbf{d}^n$  denotes the distance vector connecting two particles at  $n$ , and  $N_c$  is the total number of particles encapsulated in the volume  $V$  of the unit cell. Again,  $V$  must be large enough for Eq. (2.15) to be meaningful in the continuum sense. The stress response obtained from Eq. (2.15) is obtained directly from the grain scale mechanics and reflects the configuration and constitutive response of the grains themselves. It could be argued that Eq. 2.15 is purely physics-based and that phenomenology is not involved in its derivation. However, for reasons previously stated, the constitutive response of the granular system is typically altered in order to resolve practical problems of interest and hence (2.15) is reduced to a phenomenological approach. This deficiency can be eliminated if one focuses the computation to small regions such as the aforementioned unit cells.

When used at the appropriate scale, the main advantage of the grain scale approach, exemplified by the DEM, is the ability to bypass the phenomenological approach necessi-

tated hitherto by classical plasticity models. Its main disadvantage is the computational expense required, and related to this, the current inability to simulate complex 3D granular systems, such as natural sands. One alternative is to develop high-fidelity algorithms to capture material behavior more accurately and focus the effort on small regions. Another possibility is furnished by advanced experimental techniques combined with modern imaging. In fact, X-ray computed tomography (XR-CT) and digital image correlation (DIC) are two techniques currently being used in concert to extract very important information from experiments. Depending on the resolution, one can obtain meso scale, and even grain scale, images of the deformation in granular materials. Fig. 3 shows the grain scale configuration obtained via synchrotron XR-CT *in situ* (i.e., on site and in real time) during a triaxial compression experiment in dense sand. The image was obtained by researchers at the 3S-R Labs using the European Synchrotron Radiation Facility (ESRF) in Grenoble, France. The observed mean grain diameter was about  $300\mu\text{m}$  and the sample diameter was 11 mm. At different levels in the loading program, 3D images, such as that shown in Fig. 3(b), were obtained by stacking several slices, such as that shown in Fig. 3(a). Another example of the currently available experimental-imaging capabilities is depicted in Fig. 4 ([Lenoir et al., 2007](#)). The image was obtained using XR-CT and 3D-DIC on a sample of argillaceous rock under triaxial compression. As demonstrated in the figure, the technique allows for accurate calculation of the strain field at the meso (continuum) scale.

Either via grain scale computations (e.g., using DEM) or using advanced experimental techniques enhanced by imaging capabilities, the time is ripe to look at the microstructure in areas of interest, for example shear bands, and probe the microstructure to obtain high-fidelity material parameters. These parameters stemming directly from the microstructure can be used at the continuum scale, perhaps in lieu of phenomenologically driven ones. The next section outlines this concept further for the class of plasticity models presented in the previous sections.

## 3. Multiscale framework

In this section, a simple framework is proposed for coupling grain scale mechanics, stemming from computations

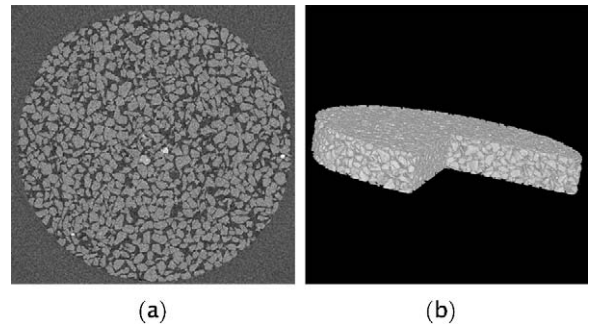


**Fig. 3.** Grain scale imaging using synchrotron XR-CT. (a) slide of sample of sand and (b) 3D reconstruction by staking slices. Original image courtesy of 3S-R Labs, Grenoble, France.

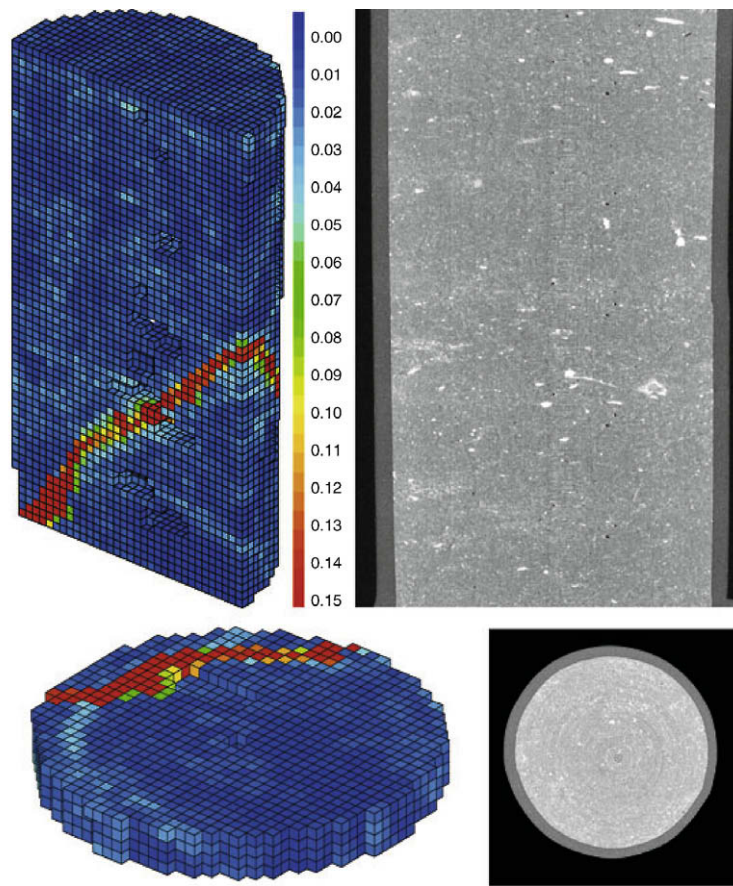


**Fig. 4.** Deformation mapping using XR-CT and 3D-DIC. Vertical cut along the axis of the specimen (top) and horizontal cut close to the bottom end of the specimen (bottom). Left (in color): deviatoric incremental strain (strain averaged over the elements; local gauge length is 280  $\mu\text{m}$ ); right: radiographic cut just after the peak deviator stress. After Lenoir et al. (2007). (For interpretation of the references to color in this figure legend, the reader is referred to the web version of this paper.)

or high-fidelity experiments, with continuum plasticity models, such as those presented above. The proposed framework will make use of the concept of dilatancy, and the dilatancy parameter itself will be obtained directly from the microstructure. Recall the definition for the dilatancy parameter, i.e.,

$$\beta = \frac{\dot{\epsilon}_v^p}{\dot{\epsilon}_s^p} \approx \frac{\dot{\epsilon}_v}{\dot{\epsilon}_s} \quad (3.1)$$

where we have neglected the elastic strain increments to write the approximation with the total strain increments. This is a plausible approximation once plasticity dominates the deformations, which is the case for most granular materials after yielding. Therefore, the dilatancy can be extracted directly from unit cell computations or from experiments and passed directly to the plasticity model. This will eliminate the need for a phenomenological evolution law relating the dilatancy to the plastic strains. The difficulty lies in how to extract this parameter from the unit cell computations.

By the same token, the frictional resistance can be computed directly from the unit cell calculations by exploiting the stress equation given in 2.15. Hence,  $\eta$  can be calcu-

lated from the stress ratio obtained from the stress  $\bar{\sigma}$  from the DEM and passed upwards to the plasticity model without resorting to a hardening law. Alternatively, one can use a stress–dilatancy relation, such as 2.9, to update the frictional resistance as a function of the dilation resistance. Recall that the residual frictional resistance for granular materials is constant. Therefore, if the dilatancy is obtained directly from the unit cell computations, and then the frictional resistance is updated via a stress–dilatancy relation, the plasticity model only requires three material constants, i.e., Young's modulus  $E$ , Poisson's ratio  $\nu$ , and the residual frictional resistance  $\eta_{cv}$  (alternatively,  $\phi_{cv}$ ). These material constants have a very clear physical interpretation and can be obtained simultaneously from just one experiment, e.g., direct shear.

It is apparent that the success of the framework depends crucially on the correct extraction of the dilatancy from the unit cell computations. One important detail to keep in mind is that dilatancy in granular media is path-dependent. Therefore, compatibility of deformations and stresses between the macroscopic and microscopic model must be ensured. In other words, if the dilatancy at an instant in discrete time  $t_{n+1}$  is to be extracted (as done in

finite elements or finite differences), then the deformation history encapsulated in the macroscopic strain tensor  $\epsilon_n$  must be projected onto the unit cell. Fig. 5 shows the projection strategy from a region in finite element space associated with a given Gauss point onto the unit cell encapsulating the granular material. The multiscale scheme hinges on three crucial steps:

1. Projecting the recent macroscopic strain history (i.e.,  $\epsilon_n$ ) to precondition the granular matrix.
2. Probing the microstructure with *mixed* boundary conditions.
3. Computing the dilation based on Eq. (3.1) and upscaling the result.

Step 2 deserves further explanation.

As mentioned before, granular materials are path dependent. Consequently, it is not enough to precondition the unit cell (step 1), but it is necessary to probe the material with an incremental strain or stress to extract the material condition. Looking at Eq. (3.1), the first inclination would be to probe the material using the incremental strain  $\Delta\epsilon$ . This would be the simplest alternative and would resemble the strain-driven procedure followed by material subroutines, i.e., given  $\epsilon_n$  and  $\Delta\epsilon$ , obtain the current stress  $\sigma_{n+1}$ . Unfortunately, for purposes of extracting the dilation, imposing the incremental strain  $\Delta\epsilon$  fully would overconstrain the solution, in essence prescribing the dilation *a priori*. Therefore, mixed boundary conditions are required. Nevertheless, the matrix must be probed with an incremental strain sufficiently close to the actual deformation. One alternative is to discard the vertical component of the deformation (e.g.,  $\Delta\epsilon_{22}$  in 2D) and apply the corresponding stress component from the preconditioned configuration. Fig. 5 shows an example of such mixed boundary conditions in 2D, resembling the direct shear configuration.

**Remark 2.** It is tempting to try to impose incremental stress probes to circumvent the issue of overconstraining the dilatancy associated with strain-driven probes. Unfortunately, stress-driven probes also lead to overconstrained

systems, basically prescribing the frictional resistance *a priori*. On the other hand, mixed boundary conditions yield independent stress-dilatancy evolutions.

**Remark 3.** The projection/upscale scheme presented above is one possible alternative to extracting dilation in a multiscale framework. However, other procedures that account for the path dependence of the material and, therefore, implicitly or explicitly contain steps 1 through 3 outlined above, would yield similar results. For instance, homogeneous elemental responses from high fidelity experiments (e.g., triaxial compression) can be directly used to extract the dilatancy evolution of the material. Similarly, DIC techniques can be used to extract deformation histories in materials and to calculate dilation evolution in space. Both of these techniques can be used to extract dilation behavior from granular materials directly, without invoking a micromechanical model. All of the aforementioned techniques are explored in the numerical examples presented in this work.

#### 4. Numerical implementation

The numerical implementation of the proposed multiscale framework is mainly composed of two sequential steps:

- STEP 1. Unit cell calculation of the dilation and friction resistance (element level).  
STEP 2. Integration of stresses using isotropic plasticity (material or Gauss point level).

The implementation of these two steps is not difficult and different procedures may yield similar results. For example, the dilation and friction resistance (e.g.,  $\beta$  and  $\mu$ ) can be extracted from unit cells of various sizes. The unit cell can be selected to cover a representative area around a Gauss integration point, as shown in Fig. 5, resembling the local Quasi-Continuum strategy (Tadmor et al., 1996). Alternatively, the whole finite element can be taken as a unit cell, or the unit cell can be allowed to cover multiple elements, resembling the non-local Quasi-Continuum. The size of the unit cell is ultimately guided by the physical length scale associated with the problem and the available computational power.

A schematic of STEP 1 in the multiscale algorithm is shown in Fig. 6. Calculation of dilatancy requires application of an incremental deformation under mixed boundary conditions (B.C.s) (e.g., direct shear). Application of purely strain driven conditions would over-constrain the system and effectively prescribe the value of dilatancy. By the same token, the ‘probe’ or the application of the mixed B.C.s must closely reflect the imposed macroscopic deformations since the dilatancy depends on the current state and the incremental deformations.

As shown in Fig. 6, the first step is to precondition the granular assembly represented in the unit cell by projecting the macroscopic deformations from the finite element computations. This can be achieved by introducing ghost nodes and imposing the deformation history reflected by

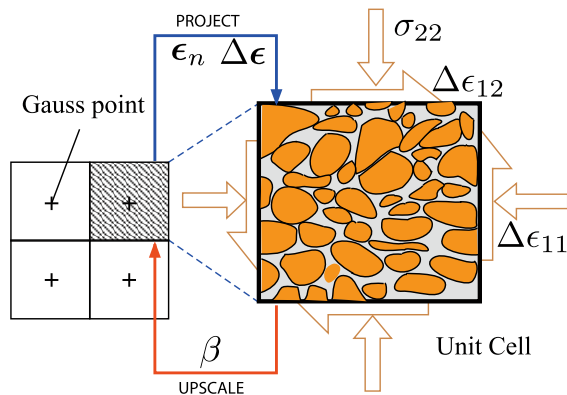


**Fig. 5.** Multiscale concept: the macroscopic strain history (up to  $t_n$ ) is superimposed on the unit cell, which is then probed – using mixed boundary conditions – to obtain and upscale the dilatancy  $\beta$ .



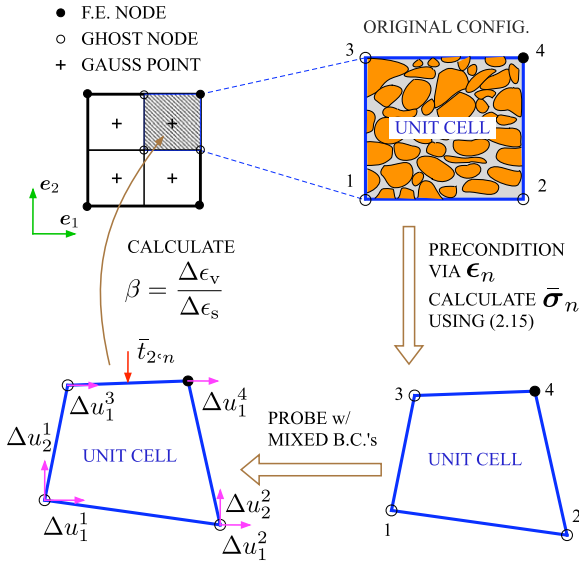


Fig. 6. Schematic illustrating STEP 1 to extract dilatancy (and friction) from grain scale.

the nodes and using the interpolation functions available from the finite elements. For example, in the case of isoparametric quads, bilinear interpolation can be used to impose the deformation from the nodes onto the boundaries. In effect, the strain history  $\epsilon_n$  is projected onto the unit cell. Due to the deformation imposed via  $\epsilon_n$ , an average stress  $\bar{\sigma}_n$  is induced that can be computed using Eq. (2.15). We note this stress is an average quantity and stems directly from the granular assembly and may not necessarily coincide with the stress obtained from the material subroutine at a Gauss integration point.

Following the preconditioning step, a ‘probe’ to the granular assembly is furnished by partially applying the incremental strains  $\Delta \epsilon$  in a similar fashion to the preconditioning step. However, as mentioned earlier, the incremental strain cannot be fully imposed, so some degrees of freedom must be allowed for the granular material to naturally dilate. One way to do this is to arbitrarily choose to apply tractions in the vertical direction using the calculated stresses from the preconditioning step. The tractions on the face of the unit cell are easily computed using Gauss theorem, i.e.,  $\bar{t}_n = \mathbf{n} \cdot \bar{\sigma}_n$ , where  $\mathbf{n}$  is the normal to the face in question. As shown in Fig. 6, vertical confinement is applied via  $\bar{t}_{2,n} = \mathbf{e}_2 \cdot \bar{t}_n$  and the incremental displacement is prescribed in all degrees of freedom, except for the vertical displacements of the top nodes (local nodes 3 and 4) where the incremental displacements are unknowns (i.e.,  $\Delta u_3^2$  and  $\Delta u_4^2$  are unknowns). Consequently, the dilatancy is obtained independently and its value reflects the current state of the fabric and the incremental deformation being imposed. Finally, the value of dilatancy  $\beta$  obtained is used to update the frictional resistance via equation 2.9 and both of these quantities are upscaled back to the Gauss integration point to be used in the material subroutine.

Given the upscaled values of  $\mu$  and  $\beta$  (or equivalently  $\phi$  and  $\psi$ ), a typical stress integration algorithm or material subroutine can be invoked. STEP 2 of the proposed multi-

scale algorithm deals with the numerical integration of the stresses to obtain a numerical solution to Eq. (2.1), which is, in general, nonlinear. The main difference with traditional stress integration algorithms stems from the choice of perfect plasticity to avoid the determination of an appropriate hardening modulus. The perfect plasticity formulation circumvents the need for a hardening law, which typically hinges on phenomenology. Instead, in the framework presented herein, the key material plasticity parameters, dilatancy and friction, are obtained using unit cell calculations in STEP 1. Consequently, the stress integration algorithm boils down to: for a given state at time  $t_n$ , encapsulated in the stress  $\sigma_n$  (or equivalently  $\epsilon_n$ ) and the plastic variables (e.g.,  $\mu$  and  $\beta$ ), find the stress state  $\sigma_{n+1}$  at time  $t_{n+1}$  induced by the strain increment  $\Delta \epsilon$ .

There are many well-established implicit integration algorithms for two- and three-invariant plasticity models (see for example Borja et al., 2003; Borja and Andrade, 2006; Andrade and Borja, 2006). Any of these integration techniques can be used, provided the plastic variables are given. In Box 1, we outline the stress-integration algorithm for the two-invariant model proposed above. In the case of plasticity developing (the case of interest here), the stresses are resolved without iteration by straightforward calculation of the plastic increment as shown in Fig. 7. For cohesionless materials, the location of the yield surface is fully described by the frictional resistance parameter  $\mu$  and since this is given from STEP 1, the plastic corrector takes the simple form

$$\Delta \lambda = \frac{\mathbf{f}_{n+1} : \mathbf{c}^e : \Delta \epsilon}{\mathbf{f}_{n+1} : \mathbf{c}^e : \mathbf{g}_{n+1}} \quad (4.1)$$

where

$$\begin{aligned} \mathbf{f}_{n+1} &= \frac{1}{3} \mu \mathbf{1} + \sqrt{\frac{3}{2}} \hat{\mathbf{n}}_{n+1} \\ \mathbf{g}_{n+1} &= \frac{1}{3} \beta \mathbf{1} + \sqrt{\frac{3}{2}} \hat{\mathbf{n}}_{n+1} \end{aligned} \quad (4.2)$$

and one can show that  $\hat{\mathbf{n}}_{n+1} = \mathbf{s}_{n+1}^{\text{tr}} / \|\mathbf{s}_{n+1}^{\text{tr}}\|$ . Therefore, everything appearing in Eq. 4.1 is given and constant. Finally, the correct stresses are computed such that

$$\sigma_{n+1} = \sigma_{n+1}^{\text{tr}} - \underbrace{\Delta \lambda \mathbf{c}^e : \mathbf{g}_{n+1}}_{\text{plastic corrector}} \quad (4.3)$$

#### Box 1: Return mapping algorithm for two-invariant perfect plasticity

1. Calculate trial stress:  $\sigma_{n+1}^{\text{tr}} = \sigma_n + \mathbf{c}^{\text{ep}} : \Delta \epsilon$
2. Check if yielding:  $F(\sigma_{n+1}^{\text{tr}}, \alpha_{n+1}) \geq 0$ ? No, set  $\sigma_{n+1} = \sigma_{n+1}^{\text{tr}}$  and exit
3. Yes, solve for plastic increment:  $\Delta \lambda = (\mathbf{f}_{n+1} : \mathbf{c}^e : \Delta \epsilon) / (\mathbf{f}_{n+1} : \mathbf{c}^e : \mathbf{g}_{n+1})$
4. Compute corrected stress:  $\sigma_{n+1} = \sigma_{n+1}^{\text{tr}} - \Delta \lambda \mathbf{c}^e : \mathbf{g}_{n+1}$

**Remark 4.** One tempting alternative would be to extract the stress state directly from the unit cell computation in STEP 1 such that  $\bar{\sigma}_{n+1}$ , obtained from Eq. (2.15), is assigned directly as the stress state at the Gauss point. The advantage of this would be that STEP 2 is completely

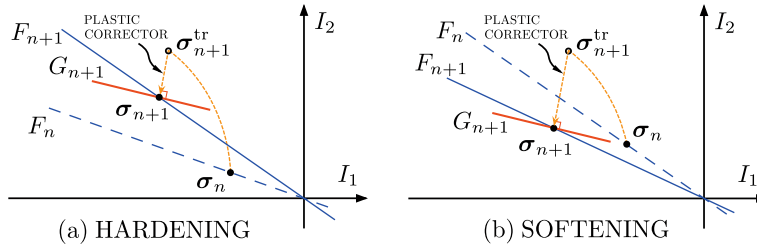


Fig. 7. Return mapping algorithm in two-invariant space.

bypassed. However, the profound disadvantage is that, since Eq. (2.15) is not a rate equation, a consistent tangent operator cannot be obtained in closed form, in general. A consistent tangent could be computed numerically, but the stress states obtained from Eq. (2.15) are, in general, nonsmooth, making the numerical calculation of tangents a nontrivial task. In contrast, the presented framework fully exploits all the tools available to computational plasticity and the smoothness properties of well-established plasticity models.

**Remark 5.** The apparent cohesion present in the plastic potential  $G_{n+1}$  is calculated to allow the yield surface and plastic potential to intersect at stress state  $\sigma_{n+1}$ , as shown in Fig. 7.

## 5. Representative numerical results

In this section, the multiscale framework presented above is used to capture the behavior of granular media under homogeneous and inhomogeneous deformations. Three simulations are performed where the multiscale technique is shown to realistically extract the material behavior from physical experiments and numerical computations. These proof-of-concept computations demonstrate the accuracy, simplicity, and versatility of the method in predicting the behavior of granular media using a unified framework, requiring the calibration of only three material constants (i.e.,  $E$ ,  $\nu$ ,  $\phi_{cv}$ ) and the extraction of the dilatancy evolution directly from the grain scale. The predictiveness of the method is assessed using advanced experiments in sands and DEM computations. Furthermore, the accuracy and simplicity of the proposed method is compared with that of an advanced phenomenological model for sands.

### 5.1. Homogeneous deformation: true triaxial experiments

The purpose of this numerical example is to demonstrate the ability of the model to extract material behavior from the granular scale using elemental physical experiments. High-fidelity physical experiments can be seen as tacit surrogate unit cell computations within the proposed framework, which constitutes a clear advantage of the method. Hence, STEP 1 of the multiscale algorithm is achieved using experiments, seeing the homogenous sample as a unit cell.

To test the multiscale framework, true triaxial experiments performed by Lade and Kim (1988) on dense Monterey No. 0 sand were used. The samples were compacted to a relative density of approximately 98%, isotropically consolidated to 60 kPa and then sheared along a variety of linear stress paths. Since the consolidation histories were identical for each test, this data set highlights the effect of the loading paths on the soil response. The stress/strain conditions of a true triaxial test are illustrated in Fig. 8. The stress path for each test is described by a constant  $B$ -value, where

$$B = \frac{\sigma_3 - \sigma_2}{\sigma_3 - \sigma_1} \quad (4.4)$$

The minor stress,  $\sigma_3$ , was held constant for each test; therefore,  $B = 0$  represents triaxial compression (TXC) and  $B = 1$  represents triaxial extension (TXE).

Three linear stress paths were considered:  $B = 0$  (TXC),  $B = 1$  (TXE), and  $B = 0.5$ . The three stress paths followed in the experiments and computations are shown in Fig. 9. This wide range of stress paths typically challenges phenomenological models, especially those incapable of accounting for the third-stress invariant  $I_3$ , e.g., Drucker–Prager. Thus, we chose the Matsuoka–Nakai model presented in Section 2.3, to highlight the importance of the third stress invariant in granular media and to underscore the flexibility of the multiscale model to accommodate two- or three-invariant models equally well. Furthermore, since the initial conditions prior to shearing were identical for each test, the model parameters were likewise identical for each simulation, with  $E = 1.2 \times 10^5$  kPa,  $\nu = 0.3$  and  $\tan \phi_{cs} = 0.8$ . These parameters are extracted from the TXC test and held constant during the simulations. The only material parameter allowed to vary is the dilatancy  $\beta \approx 2 \sin \psi$ , extracted directly from the experiments and whose evolution is shown in Fig. 10. The value of the dilatancy is updated at every time step in the computation

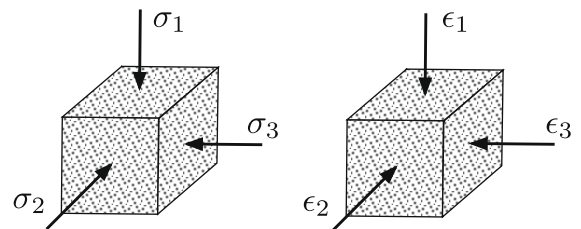


Fig. 8. Stress/strain conditions for true triaxial tests.

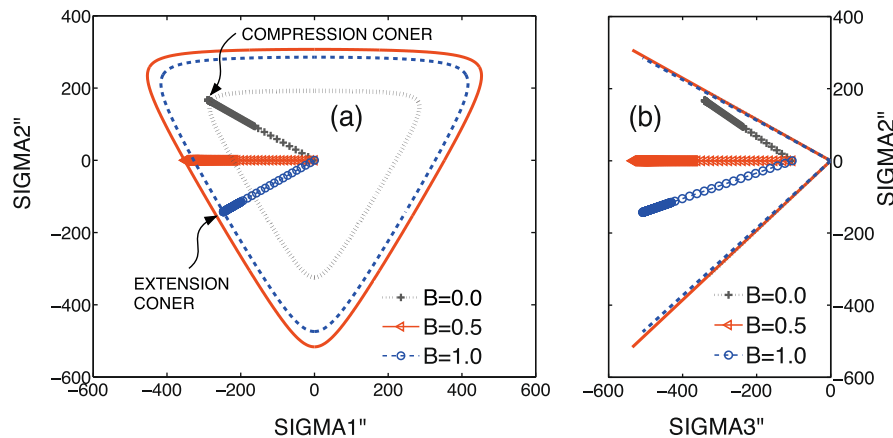


Fig. 9. Computed stress paths for true triaxial tests: (a) deviatoric plane; (b) meridian plane.

while Eq. (2.14) is used to update the friction angle  $\phi$ . Application of STEP 2 in the multiscale algorithm is performed under perfect plasticity (i.e.,  $\phi$  and  $\psi$  are held constant for a given time step) and the stresses are integrated using standard three-invariant return mapping algorithms, such as those proposed in Borja et al. (2003) and Andrade and Borja (2006).

Fig. 9 shows the computed stress paths in the deviatoric and meridian planes, respectively, where  $\sigma_1'', \sigma_2''$  and  $\sigma_3''$  are the rotated axes, which are functions of the principal stress axes  $\sigma_1, \sigma_2$  and  $\sigma_3$ , while  $\sigma_3'' \propto I_3$  corresponds to the hydrostatic stress state (Borja et al., 2003). The linear stress paths are accompanied by their corresponding yield surfaces at the end of the simulations. Fig. 9a shows the stress path on the deviatoric plane and highlights the different intersection points with the yield surface. The difference in strength in compression and extension is captured very well by the triaxiality of the yield surface. From the stress paths on the meridian plane shown in Fig. 9b, it can be noted that the friction angles at the end of the computations happen to be very close to each other. This is not a coincidence as the dilation angles are very close toward

the end of the simulations (see Fig. 10). Incidentally, computations using the Drucker–Prager model necessitate three different values for  $\tan \phi_{cs}$  in order to match the experimental results correctly. This is not only unphysical, but inconvenient from a predictive standpoint.

Fig. 11 shows the predicted stress–strain curves for all three stress paths. We emphasize that these predictions are made using the same constant parameters  $E, \nu$ , and  $\phi_{cv}$ , while extracting the evolution of the dilatancy from the experimental results (i.e., Fig. 10). Furthermore, a direct comparison is made with the predictions obtained using a phenomenological model proposed by Andrade and Borja (2006). The results obtained using the phenomenological model are the outcome of a study to evaluate the predictive-ness of the model (Andrade and Ellison, 2008). Fig. 11 clearly shows that both the multiscale and the phenomenological model capture the experimental stress–strain data very well. The phenomenological model was calibrated under TXE and nine constants were necessary to perform a prediction. This is to be contrasted with the three constants needed for the multiscale model, which have the great advantage of having clear physical interpretations. All parameters in the phenomenological model have physical interpretations, except for the hardening constant, which is simply selected to fit the data effectively.

The predicted volumetric strains are also compared with the experimental results. As shown in Fig. 12, the comparisons are as favorable as in the case of the stress–strain curves. This is not straightforward and depends on several factors, including: nonassociativity of plastic strain flow, triaxiality, the stress–dilatancy relation, etc. In other words, it is entirely possible for a model to predict the stress–strain behavior well and not do a good job at predicting the volumetric strains, and vice-versa. It is therefore important to look at both predictions in concert. The multiscale model and the phenomenological model capture the total volumetric strains equally well.

These results show the ability of the multiscale model to capture different stress paths and extract information directly from homogeneous experiments in granular materials. These advantages can be exploited in the development of more robust models for granular materials.

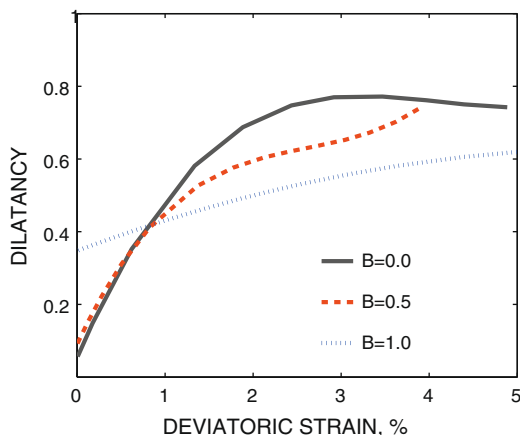
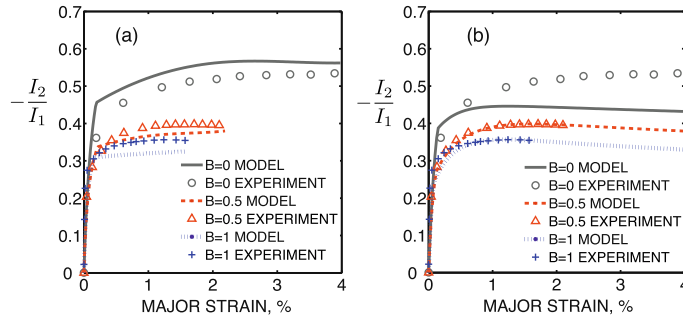


Fig. 10. Dilation evolutions for each of the linear stress paths, extracted directly from experimental results.



**Fig. 11.** Stress ratio  $-I_2/I_1$  vs.  $\epsilon_1$ : (a) predictions using multiscale model and (b) predictions made using the (Andrade and Borja, 2006) phenomenological model, after Andrade and Ellison (2008).

Nevertheless, the model can also be used in conjunction with granular mechanics models as illustrated in the next numerical example.

### 5.2. Homogeneous deformations: DEM-based unit cell

In this section, the numerical recipe shown in Section 4 is explicitly exploited to extract material behavior directly from the granular assembly. The original configuration of the granular assembly is presented in Fig. 13. This 3D assembly is loaded under triaxial compression and its behavior is simulated directly using the discrete element method. The results from the DEM calculations can be seen as direct numerical simulations (DNS) and, hence, the success or accuracy of the multiscale method will be judged by how well it can replicate the DNS results. Furthermore, the multiscale method is independent from the use of stress-dilatancy relations, such as those presented in Eqs. (2.9 and 2.14). It is clearly shown that the method can accurately extract the friction coefficient  $\mu$  and dilatancy  $\beta$  independently. This example showcases the ability of the method to extract material behavior on the fly.

The granular assembly is consolidated to an initial packing density of 0.345 using a hydrostatic pressure of 860 kPa. After the consolidation step, the lateral walls of the sample are held at constant pressure, while the top face is moved uniformly downwards. The bottom face is not al-

lowed to displace vertically. The stress–strain response for the DEM calculations are shown in Fig. 15. Using identical boundary conditions, one isoparametric ‘brick’ element (8 displacement nodes) was used to implement the multi-scale computations using the Drucker–Prager model. Since the response is homogeneous, the extracted parameters, i.e.,  $\mu$  and  $\beta$  are used in all eight Gauss points. As in the previous example, the dilatancy is extracted from the DEM code at every step in the FEM computation. The constant material parameters used in the multiscale computations are  $E = 300$  MPa,  $\nu = 0.25$  and  $\eta_{cv} = 0.6$ .

As mentioned earlier, the effects of using the stress–dilatancy relation (Eq. (2.9)) are highlighted in this example. To this end, Fig. 14 shows the dilatancy evolution for two cases: multiscale computations using the stress–dilatancy relation and multiscale computations without the stress–dilatancy relation. The multiscale method is able to extract the dilatancy and friction coefficients independently, exploiting the definition of the friction coefficient as  $2\eta = -3\sqrt{6}I_2/I_1$  (see Section 2.2). In other words, Eq. (3.1) is used to extract  $\beta$  and Eq. (2.15) is used to extract  $\eta$  independently from the DEM computations, achieving STEP 1 in the multiscale procedure. As explained earlier,

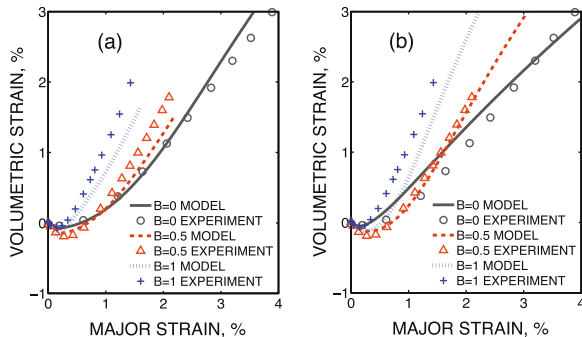


**Fig. 12.** Total volumetric strains  $\epsilon_v$  vs.  $\epsilon_1$ : (a) predictions using multiscale model and (b) predictions made using the (Andrade and Borja, 2006) phenomenological model, after Andrade and Ellison (2008).

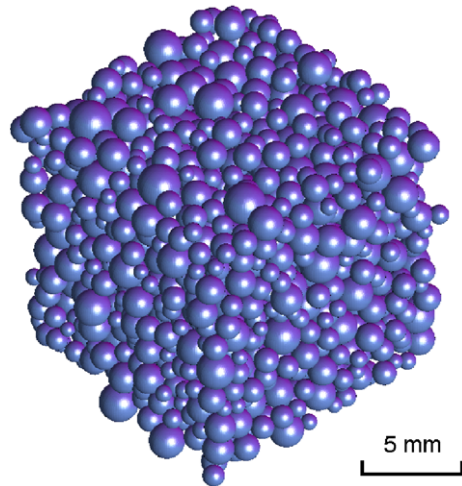


**Fig. 13.** Initial configuration of granular assembly loaded under TXC using 3D DEM.



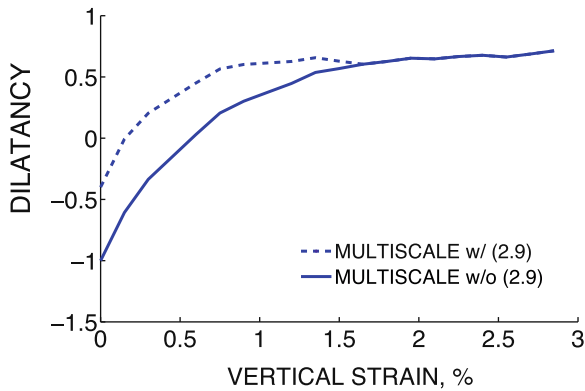


Fig. 14. Dilatancy evolutions extracted from DEM.

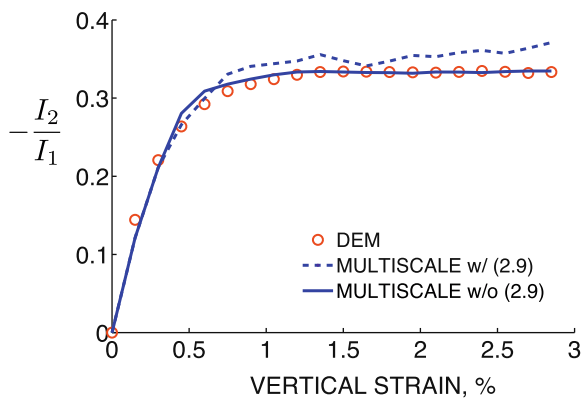


Fig. 15. Stress ratio  $-I_2/I_1$  vs. vertical strain comparing DEM and multiscale responses.

the method enjoys this capability as a direct consequence of the mixed boundary conditions applied in STEP 1 of the computation (see Section 4).

The extracted dilatancies shown in Fig. 14 differ due to an elastic correction applied to the multiscale procedure using the stress–dilatancy relation. Since the stress–dilatancy condition couples the friction coefficient with the dilatancy, negative values of dilatancy (e.g.,  $\beta = -1$ ) could result in negative values of friction  $\eta$ , which would be unrealistic. To correct this, the dilatancy is adjusted by effectively removing the elastic compressibility contributions, which are significant in the early stages of the computation. After about 1.5% axial strain, when the plastic deformations dominate, the dilatancies for the two procedures coincide as shown in Fig. 14. On the other hand, the coupling between the friction and the dilation is not present in the procedure without the stress–dilatancy relation and, hence, the evolution latter needs not be corrected.

The stress–strain relations obtained by the two multiscale procedures are compared with that obtained by DEM in Fig. 15. It is apparent that both methods compare very favorably with the results from the DNS. However, the additional degree of freedom introduced by calculating the friction coefficient  $\mu$  directly from the DEM, affords the

method without stress–dilatancy superior accuracy. Essentially, the stress–strain relations obtained by the multiscale method, without stress–dilatancy relation, and that obtained from DNS, match exactly throughout the computations. Furthermore, the responses from the different multiscale methods differ in smoothness. The method using the stress–dilatancy condition shows rougher stress–strain responses induced by the relatively rougher dilatancy evolution.

Fig. 16 shows the volumetric strain evolution results for the two multiscale methods, again compared with the DNS results. It can be seen that the evolution of the total volumetric strain is captured very accurately by both multiscale methods. As in the stress–strain results, the volumetric strains obtained by the method without stress–dilatancy are superior in accuracy to those obtained by the multiscale method using the stress–dilatancy relation. This is not too surprising as the method without stress–dilatancy effectively features a higher degree of flexibility, extracting two key material parameters independently. Unfortunately, this technique without the stress–dilatancy relation can only be applied to situations where the stress values can be extracted independently (e.g., DEM computations).

In the near future, coupling of DEM techniques to enhance FEM methods in areas of intense deformation will be achievable. Computation of material behavior at the granular level can be performed on the fly and can be coupled with the FEM codes using the techniques presented herein. In what follows, the multiscale technique is used to extract inhomogeneous behavior of granular media undergoing shear banding phenomena.

**Remark 6.** The unit cell, representing the granular assembly, requires a number of parameters to describe the micromechanical response accurately. For the DEM model, these parameters include particle geometry, grain stiffness, intergranular friction, etc. These parameters substantially determine how accurately the micromechanical model captures the true material behavior, which, however, is not the main focus of this paper. The goal of the multiscale scheme is to faithfully reproduce the response of the underlying micromechanical model at the continuum

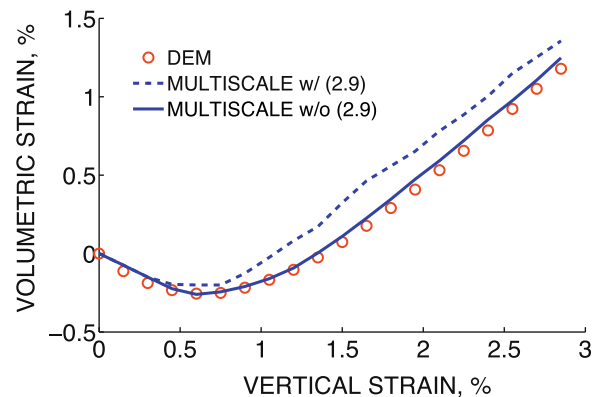


Fig. 16. Volumetric strains  $\epsilon_v$  vs. vertical strain.

scheme (whatever that micromechanical model is). Hence, the multiscale method provides a bridge from the microscale to the macroscale but it does not provide a micromechanical model. However, it is our belief that this multiscale technique will allow further development of accurate and physics-based micromechanical models in the near future.

**Remark 7.** A crucial item to the success of the proposed multiscale technique is the appropriate selection of the minimum size of the unit cell. In this work, we have not invoked any theoretical basis for the selection of the size, but rather have based our determination on the concept of the unit cell (and RVE for that matter), that it is the minimum size element where high oscillations in continuum properties can be filtered out. Subsequent increases in the size of the unit cell did not yield significant differences in the results.

### 5.3. Inhomogeneous deformations: shear banding in dense sands

As stated in the Introduction, one of the most promising areas of application for multiscale techniques, such as the one presented in this manuscript, is in the prediction and simulation of deformation bands. Phenomenological models are incapable of accessing the material behavior inside a deformation band and, hence, post-bifurcation analysis cannot be accurately performed given the current technology. Ultimately, the multiscale model presented herein will allow for such post-bifurcation analysis. However, micromechanical models will have to be enhanced to capture the complex behavior of real granular materials such as sands. For instance, it is well known that angularity or shape of particles is intimately related to the dilatancy in granular materials (Mirghasemi et al., 2002; Procopio and Zavalianos, 2005). Therefore, classic grain scale methods, such as DEM, using spherical particles cannot accurately represent the behavior of complex geomaterials. In fact, a micromechanical method able to capture the behavior of a granular

assembly, such as the one presented in Fig. 3, has yet to emerge. Multiscale methods will play a crucial role in the development of more accurate micromechanics as they allow for more refined computation in a selective fashion. In the meantime, the proposed multiscale model presented herein can be used in conjunction with advanced experiments to extract material behavior in high deformation zones and under inhomogeneous conditions. In the near future, this extraction will be performed computationally.

As a proof-of-concept of the proposed technique, we analyze the behavior of a physical experiment in dense sand under plane strain conditions. The experiments were conducted by Mooney (1996) and Mooney et al. (1998) on masonry sand and were instrumented using lateral LVDTs. Stereophotogrammetry was used once homogeneity was lost to extract a deformation field. From the deformation field, Mooney et al. (1998) extracted the dilation angle across the specimen. Fig. 17a shows the evolution of the dilation angle as a function of axial compressive strain. The sample was initially consolidated anisotropically with axial stress  $\sigma_1 = -210$  kPa and lateral stresses  $\sigma_2 = \sigma_3 = -105$  kPa. After consolidation, the sample was failed under plane strain while keeping the lateral stress  $\sigma_3$  constant. The other two components of stress were measured using instrumentation. At about 3% axial compressive strain the sample developed a persistent shear band about 4 mm thick at about  $63^\circ$  from the horizontal as shown in Fig. 17b. After the bifurcation was observed, the deformation localized to the shear band and the dilation angle was measured locally inside the band using stereophotogrammetry. The values reported in Fig. 17a are average values across the band and assume uniform conditions into the plane. The interested reader is referred to Mooney (1996) and Mooney et al. (1998) for more information regarding the experimental setup and results.

To simulate this boundary value problem, the location and the orientation of the shear band were prescribed *a priori* in a finite element mesh based on the experimental data. The two-invariant Drucker–Prager model was used to represent the material behavior. For the entire sample,

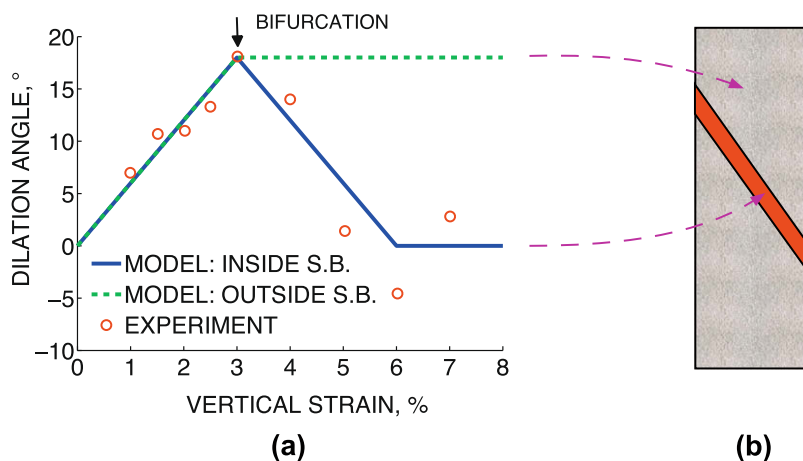


Fig. 17. Dilation angle measured in the plane strain test and dilation relations used for materials inside and outside the prescribed shear band.

the same set of parameters was used, with  $E = 4 \times 10^4$  kPa,  $\nu = 0.2$ , and  $\eta_{cv} = 1.15$ . The elastic parameters were obtained by calibration with the initial portion of the experiments, while the friction coefficient at constant volume was determined using the plastic portion of the data. The dilation relation represented by the solid line in Fig. 17a was used for the material within the prescribed shear band, while the relation along the dashed line was used for the rest of the simulated sample. The sample outside the shear band was observed to unload elastically, while all plastic deformations localized inside the band. Therefore, the assumption of a constant dilation angle for the material outside the band is immaterial. The prescribed evolution of the dilation angle allows for an accurate capture of the material response and eliminates the need to perform an accurate evaluation of the localization condition. Nevertheless, we will show that bifurcation – signaled by the Rudnicki–Rice condition – is achieved one time step after the material parameters are allowed to bifurcate due to the sudden loss of homogeneity in the sample.

Fig. 18 shows the computed distribution of deviatoric strain in the deformed mesh at  $\epsilon_1 = 7\%$ . The sample was discretized using a coarse mesh of 20 isoparametric bilinear quadrilaterals. As expected, post-bifurcation, the strains are completely localized inside the deformation band while the deformations inside the band are homogeneous and close to simple shear. Additionally, Fig. 19 shows the determinant of the acoustic tensor recorded at a Gauss point within the prescribed shear band. It is well known that the acoustic tensor is strongly dependent on the material response and its explicit definition can be found in Rudnicki and Rice (1975) and in Andrade and Borja (2006). As shown in Fig. 19, the observed onset of the shear band corresponds with the loss of positive definiteness of the acoustic tensor, which is consistent with the

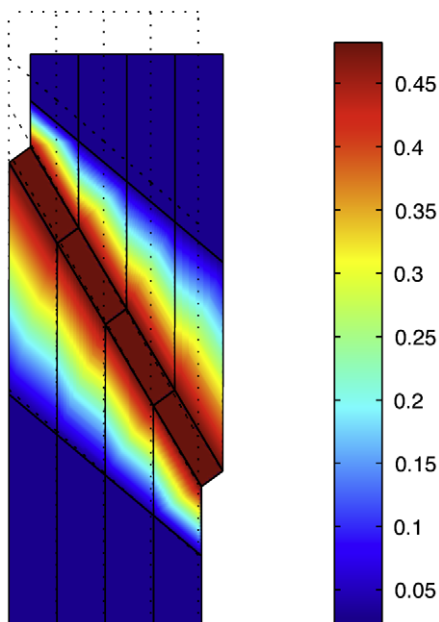


Fig. 18. Computed deviatoric strain distribution at  $\epsilon_1 = 7\%$  (20 elements).

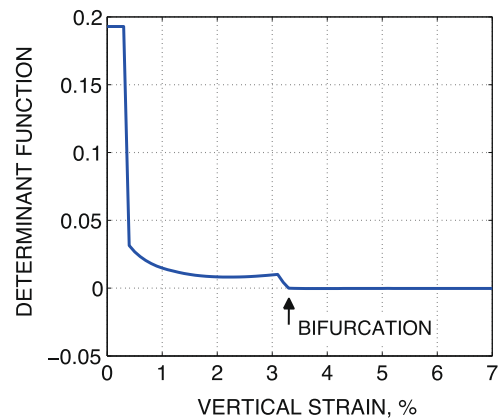


Fig. 19. Determinant of acoustic tensor computed within shear band.

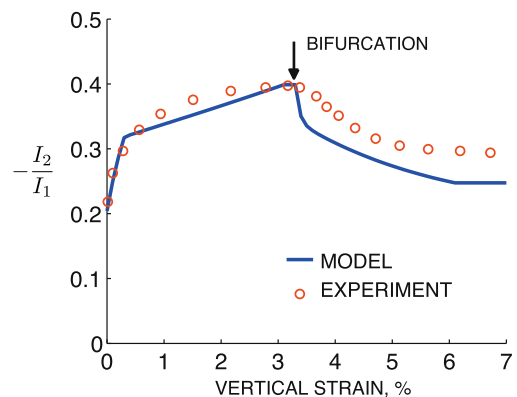


Fig. 20. Observed and computed evolution of stress ratio.

classical bifurcation theory, i.e., bifurcation or strain localization occurs when the determinant of the acoustic tensor drops below zero (Rudnicki and Rice, 1975).

Fig. 20 shows the observed and computed evolution of the stress ratio  $-I_2/I_1$  where the values reported correspond to the global stresses applied to the boundaries of the specimen, and only reflect the state of stress on average. In the computation, the material outside the shear band experienced elastic and homogenous unloading during the postlocalization stage. The ‘elastic’ portion of the stress–strain curve can be seen from the figure. This portion was used to obtain the elastic constants required by the model. The friction coefficient at constant volume was obtained from the asymptotic portion of the data (near 7% vertical strain). Since these are material constants, it would be possible to use them in predicting the behavior of another sample of sand with similar initial conditions, but perhaps different boundary conditions, e.g., TXC. In any case, the only variable in the simulation is the dilation angle, taken from Fig. 17a and extracted directly from the granular structure. It is clear from Fig. 20 that the multi-scale model does an excellent job both pre- and post-bifurcation. The peak stress ratio and the softening branch are captured remarkably well.

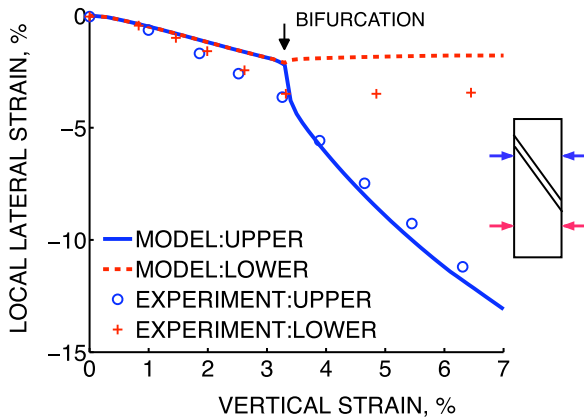


Fig. 21. Observed and computed local lateral strains.

Even though the stress–strain results are reassuring, it is equally important and challenging to capture the deformations accurately. As in the homogeneous case, it is possible to postulate a model that captures the stress–strain curve well, but completely misses the kinematics of deformation and vice-versa. Fig. 21 shows the computed and measured local lateral strains. In the physical experiment, two pairs of horizontal LVDTs were placed on the sample to measure the local lateral strains as shown in Fig. 21. It is possible to see that the sample deforms homogeneously pre-bifurcation, with both the top and bottom parts dilating equally. However, post-bifurcation, the bottom part remains rigid while the top part ‘slides’ as a rigid block, concentrating all deformations in the shear band. The multiscale model successfully captures both pre- and post-bifurcation deformation patterns, which is quite remarkable given the simplicity of the model.

It is well-known that rate-independent plasticity models exhibit pathologic mesh dependence post-bifurcation (Bažant and Belytschko, 1985; Borja, 2000). Hence, we performed a mesh sensitivity study to quantify the mesh dependence of the obtained results. Fig. 22 shows a comparison of results from two computations using different meshes. The coarse mesh comprises 20 elements, while the fine mesh is a consistent refinement of the coarse mesh and contains 80 isoparametric bilinear elements. All other

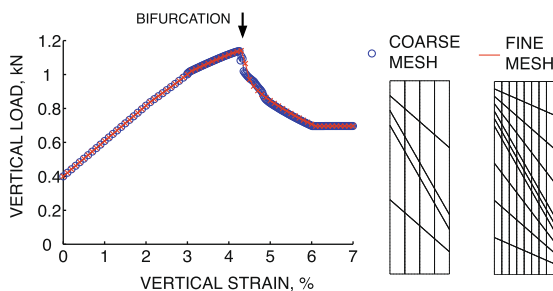


Fig. 22. Comparison of computed results using two different meshes.

conditions, including material parameters, are identical. As shown in Fig. 22, the computed vertical loads are close to each other throughout these two computations, indicating that the calculated loads in FEM simulations are not sensitive to the mesh in the context of the prescribed localization. However, the deformation pattern is mesh sensitive, with the width of the shear band localizing to one element, as expected (Bažant and Belytschko, 1985).

**Remark 8.** It is expected that the proposed multiscale framework will exhibit mild mesh dependence, if any, as the extracted material parameters (e.g.,  $\phi$  and  $\psi$ ) are rate-dependent by virtue of the material length scale inherently present in true granular assemblies and in particle mechanics models, such as DEM. In other words, the generalized Hooke’s law given in Eq. (2.1) is no longer independent of the strain rate and should now read:  $\dot{\sigma} = \mathbf{c}^{\text{ep}}(\epsilon, \dot{\epsilon}) : \dot{\epsilon}$ . This rate-dependence is expected to regularize the solution. This regularization is not present in the results presented above as the material behavior was extracted from the experimental results rather than direct numerical simulations.

## 6. Conclusions

We have presented a simple predictive multiscale model for the mechanical behavior of granular media. The model fully exploits the current finite element and computational inelasticity technology, but bypasses phenomenological procedures used to update material parameters necessitated by classical plasticity models. We have shown that semi-concurrent computations linking the macroscopic scale with the granular scale, and further probing of the microstructure, lead to the extraction of two key material parameters for granular media: dilatancy and frictional resistance. The presented framework is able to extract both parameters independently or linked by using a stress–dilatancy relation. The upshot of the methodology is the possibility to enhance classical plasticity models by directly extracting dilatancy and frictional resistance from the underlying granular structure. The technique is shown to be not only simple, but applicable to a wide spectrum of loading conditions ranging from triaxial compression to triaxial extension to plane strain to full-blown boundary value problems where shear banding is observed. The method is amenable to coupling with discrete element codes, as well as high-fidelity experiments. Comparisons with experimental data and direct numerical simulations clearly highlight the predictive capability of the model. The simplicity and predictiveness of the model open the door to a new generation of predictive multiscale methods from which complex material responses can be extracted in regions where phenomenological models break down.

## Acknowledgements

Support for this work was partially provided by NSF Grant No. CMMI-0726908 and AFOSR Grant No. FA9550-08-1-1092 to Northwestern University. This support is gratefully acknowledged. The expert feedback from the



anonymous reviewers is greatly appreciated. The DEM results shown in this research were performed using *Oval*, developed by Prof. M.R. Kuhn from the University of Portland.

## References

- Anandarajah, A., 1999. Multiple time-stepping scheme for the discrete element analysis of colloidal particles. *Powder Technology* 106, 132–141.
- Andrade, J.E., 2009. A predictive model for static liquefaction. *Géotechnique*.
- Andrade, J.E., Borja, R.I., 2006. Capturing strain localization in dense sands with random density. *International Journal for Numerical Methods in Engineering* 67, 1531–1564.
- Andrade, J.E., Ellison, K.C., 2008. Evaluation of a predictive constitutive model for sands. *Journal of Geotechnical and Geoenvironmental Engineering* 134, 1825–1828.
- Barbosa-Carrillo, R.E., 1990. Discrete Element Models for Granular Materials and Rock Masses. Ph.D. thesis, University of Illinois, Urbana-Champaign, IL.
- Bardet, J.P., Proubet, J., 1991. A numerical investigation of the structure of persistent shear bands in granular media. *Géotechnique* 41, 599–613.
- Bažant, Z.P., Belytschko, T.B., 1985. Wave propagation in strain-softening bar: exact solution. *Journal of Engineering Mechanics* 111, 381–389.
- Belytschko, T., Gracie, R., Mei, X., 2008a. Bridging the Scales in Science and Engineering chapter Concurrent Coupling of Atomistic and Continuum Models. Clarendon Press.
- Belytschko, T., Loehnert, S., Song, J.H., 2008b. Multiscale aggregating discontinuities: a method for circumventing loss of material stability. *International Journal for Numerical Methods in Engineering* 73, 869–894.
- Borja, R.I., 2000. A finite element model for strain localization analysis of strongly discontinuous fields based on standard Galerkin approximation. *Computer Methods in Applied Mechanics and Engineering* 190, 1529–1549.
- Borja, R.I., 2002. Bifurcation of elastoplastic solids to shear band mode at finite strains. *Computer Methods in Applied Mechanics and Engineering* 191, 5287–5314.
- Borja, R.I., 2006. Condition for liquefaction instability in fluid-saturated granular soils. *Acta Geotechnica* 1, 211–224.
- Borja, R.I., Andrade, J.E., 2006. Critical state plasticity. Part VI: Meso-scale finite element simulation of strain localization in discrete granular materials. *Computer Methods in Applied Mechanics and Engineering* 195, 5115–5140.
- Borja, R.I., Sama, K.M., Sanz, P.F., 2003. On the numerical integration of three-invariant elastoplastic constitutive models. *Computer Methods in Applied Mechanics and Engineering* 192, 1227–1258.
- Borja, R.I., Wren, J.R., 1995. Micromechanics of granular media. Part I: Generation of overall constitutive equation for assemblies of circular disks. *Computer Methods in Applied Mechanics and Engineering* 127, 13–36.
- Cambou, B., 1998. *Behaviour of Granular Materials*. Springer, New York, NY.
- Christoffersen, J., Mehrabadi, M.M., Nemat-Nasser, S., 1981. A micromechanical description of granular material behavior. *Journal of Applied Mechanics* 48, 339–344.
- Collins, I.F., 1990. Plane strain characteristics theory for soils and granular materials with density dependent yield criteria. *Journal of the Mechanics and Physics of Solids* 38, 1–25.
- Cundall, P.A., 1988. Formulation of a three-dimensional distinct element model I: A scheme to detect and represent contacts in a system composed of many polyhedral blocks. *International Journal of Rock Mechanics and Mining Sciences* 25 (3), 107–116.
- Cundall, P.A., 2001. A discontinuous future for numerical modelling in geomechanics? *Geotechnical Engineering ICE* 149, 41–47.
- Cundall, P.A., Strack, O.D.L., 1979. A discrete numerical model for granular assemblies. *Géotechnique* 29, 47–65.
- Dafalias, Y.F., Popov, E.P., 1975. A model of nonlinearly hardening materials for complex loadings. *Acta Mechanica* 21, 173–192.
- Deen, N.G., Van Sint Annaland, M., Van der Hoef, M.A., Kuipers, J.A.M., 2007. Review of discrete particle modeling of fluidized beds. *Chemical Engineering Science* 62, 28–44.
- DiMaggio, F.L., Sandler, I.S., 1971. Material model for granular soils. *Journal of the Engineering Mechanics Division-ASCE* 97, 935–950.
- Drucker, D.C., Prager, W., 1952. Soil mechanics and plastic analysis or limit design. *Quarterly of Applied Mathematics* 10, 157–165.
- Harris, D., 1992. Plasticity models for soil granular and jointed rock materials. *Journal of the Mechanics and Physics of Solids* 40, 273–290.
- Hartley, R.R., Behringer, R.P., 2003. Logarithmic rate dependence of force networks in sheared granular materials. *Nature* 421, 928–931.
- Jefferies, M.G., 1993. Nor-S and: a simple critical state model for sand. *Géotechnique* 43, 91–103.
- Kingston, M.R., Spencer, A.J.M., 1970. General yield conditions in plane deformations of granular media. *Journal of the Mechanics and Physics of Solids* 18, 233–243.
- Kuhn, M.R., 2003. Smooth convex three-dimensional particle for the discrete-element method. *Journal of Engineering Mechanics-ASCE* 129, 539–547.
- Lade, P.V., Duncan, J.M., 1975. Elastoplastic stress-strain theory for cohesionless soil. *Journal of the Geotechnical Engineering Division ASCE* 101, 1037–1053.
- Lade, P.V., Kim, M.K., 1988. Single hardening constitutive model for frictional materials II. Yield criterion and plastic work contours. *Computers and Geotechnics* 6, 13–29.
- Lenoir, N., Bornert, M., Desrues, J., Viggiani, G., 2007. 3d digital image correlation applied to X-ray microtomography images from triaxial compression tests on argillaceous rock. *Strain* 43, 193–205.
- Lin, X., Ng, T.T., 1997. A three-dimensional discrete element model using arrays of ellipsoids. *Géotechnique* 47, 319–329.
- Liu, W.K., Karpov, E.G., Park, H.S., 2006. *Nano Mechanics and Materials*. John Wiley & Sons Ltd., Chichester, West Sussex, UK.
- Liu, W.K., McVeigh, C., 2008. Predictive multiscale theory for design of heterogeneous materials. *Computational Mechanics* 42, 147–170.
- Ma, X., Zhang, D.Z., 2006. Statistics of particle interactions in dense granular material under uniaxial compression. *Journal of the Mechanics and Physics of Solids* 54, 1426–1448.
- Marketos, G., Bolton, M.D., 2007. Quantifying the extent of crushing in granular materials: a probability-based predictive method. *Journal of the Mechanics and Physics of Solids* 55, 2142–2156.
- Matsuoka, H., Nakai, T., 1982. A new failure criterion for soils in three-dimensional stresses. In *Conference on Deformation and Failure of Granular Materials*, 253–263. IUTAM.
- McDowell, G.R., Bolton, M.D., Robertson, D., 1996. The fractal crushing of granular materials. *Journal of the Mechanics and Physics of Solids* 44, 2079–2102.
- Mirghasemi, A.A., Rothenburg, L., Matyas, L., 2002. Influence of particle shape on engineering properties of assemblies of two-dimensional polygon-shaped particles. *Géotechnique* 52, 209–217.
- Mooney, M.A., 1996. An Experimental Study of Strain Localization and the Mechanical Behavior of Sand. Ph.D. thesis, Northwestern University, Evanston, IL.
- Mooney, M.A., Finno, R.J., Viggiani, M.G., 1998. A unique critical state for sand? *Journal of Geotechnical and Geoenvironmental Engineering* 124, 1100–1108.
- Mueth, D.M., 2003. Measurements of particle dynamics in slow dense granular Couette flow. *Physical Review E* 67, 011304.
- Nova, R., Wood, D.M., 1979. A constitutive model for sand in triaxial compression. *International Journal for Numerical and Analytical Methods in Geomechanics* 3, 255–278.
- Oda, M., Iwashita, K., 1999. *Mechanics of Granular Materials: An Introduction*, A.A. Balkema, Brookfield, VT.
- Oda, M., Takemura, T., Takahashi, M., 2004. Microstructure in shear band observed by microfocus X-ray computed tomography. *Géotechnique* 54, 539–542.
- Procopio, A.T., Zavaliangos, A., 2005. Simulation of multi-axial compaction of granular media from loose to high relative densities. *Journal of the Mechanics and Physics of Solids* 53, 1523–1551.
- Rechenmacher, A.L., 2006. Grain-scale processes governing shear band initiation and evolution in sands. *Journal of the Mechanics and Physics of Solids* 54, 22–45.
- Reynolds, O., 1885. On the dilatancy of media composed of rigid particles in contact. *Philosophical Magazine and Journal of Science* 20, 468–481.
- Rowe, P.W., 1962. The stress-dilatancy relation for static equilibrium of an assembly of particles in contact. *Proceedings of the Royal Society of London A* 269, 500–527.
- Rudnicki, J.W., Rice, J.R., 1975. Conditions for localization of deformation in pressure-sensitive dilatant materials. *Journal of the Mechanics and Physics of Solids* 23, 371–394.

- Sallam, A.M., 2004. Studies on Modeling Angular Soil Particles Using the Discrete Element Method. Ph.D thesis, University of South Florida, Tampa, FL.
- Schofield, A., Wroth, P., 1968. *Critical State Soil Mechanics*. McGraw-Hill, New York.
- Severson, B. A Nano to Macro Study of Friction and Adhesion in Granular Materials. Ph.D. thesis, Northwestern University, Evanston 2007.
- Sheng, Y., Lawrence, C.J., Briscoe, B.J., Thornton, C., 2004. Numerical studies of uniaxial powder compaction process by 3D DEM. *Engineering Computations* 21 (2–4).
- Simo, J.C., Hughes, T.J.R., 1998. *Computational Inelasticity*. Prentice-Hall, New York.
- Tadmor, E., Ortiz, M., Phillips, R., 1996. Quasicontinuum analysis of defects in solids. *Philosophical Magazine A* 73, 1529–1563.
- Tavarez, F.A., 2005. Discrete Element Method for Modeling Solid and Particulate Materials. Ph.D. thesis, University of Wisconsin, Madison, CA.
- Tavarez, F.A., Plesha, M.E., 2007. Discrete element method for modelling solid and particulate materials. *International Journal for Numerical Methods in Engineering* 70, 379–404.
- Taylor, D.W., 1948. *Fundamentals of Soil Mechanics*. John Wiley & Sons Ltd, New York.
- Tu, X., Andrade, J.E., 2008. Criteria for static equilibrium in particulate mechanics computations. *International Journal for Numerical Methods in Engineering* 75, 1581–1606.
- Vermeer, P.A., de Borst, R., 1984. Non-associated plasticity for soils concrete and rock. *Heron* 29, 1–62.
- Wellmann, C., Lillie, C., Wriggers, P., 2008. Homogenization of granular material modeled by a three-dimensional discrete element method. *Computers & Geotechnics* 35, 394–405.
- Wood, D.M., 1990. *Soil Behaviour and Critical State Soil Mechanics*. Cambridge University Press, Cambridge, UK.
- You, Z., 2003. Development of a Micromechanical Modeling Approach to Predict Asphalt Mixture Stiffness Using the Discrete Element Method. Ph.D. thesis, University of Illinois, Urbana-Champaign, IL.